


Application of the Landau-Zener-Stückelberg-Majorana dynamics to the electrically driven flip of a hole spin

W. J. Pasek, M. Z. Maialle, and M. H. Degani

School of Applied Sciences, University of Campinas, Rua Pedro Zaccaria, 1300 Jardim Santa Luiza, Limeira, SP 13484-350, Brazil

 (Received 26 December 2017; published 13 March 2018)

An idea of employing the Landau-Zener-Stückelberg-Majorana dynamics to flip a spin of a single ground state hole is introduced and explored by a time-dependent simulation. This configuration interaction study considers a hole confined in a quantum molecule formed in an InSb (111) quantum wire by application of an electrostatic potential. An up-down spin-mixing avoided crossing is formed by nonaxial terms in the Kohn-Luttinger Hamiltonian and the Dresselhaus spin-orbit one. Manipulation of the system is possible by the dynamic change of an external vertical electric field, which enables the consecutive driving of the hole through two anticrossings. Moreover, a simple model of the *power-law*-type noise that impedes precise electric control of the system is included in the form of random telegraph noise to estimate the limitations of the working conditions. We show that in principle the process is possible, but it requires precise control of the parameters of the driving impulse.

DOI: [10.1103/PhysRevB.97.115417](https://doi.org/10.1103/PhysRevB.97.115417)

I. INTRODUCTION

Electric dipole spin resonance (EDSR) is a process in which the spin state of a quantum system is manipulated by means of an ac electric field [1–11]. This process can utilize a few different mechanisms of electric-spin coupling: the spin-orbit interaction [1,3,6–8,10,11], the spatial inhomogeneity of the applied magnetic field [2,5], or of the hyperfine interaction [4]. If the frequency of the electric signal is resonant to the relevant energy difference of two levels with different spin, then a transition between the levels may be induced, depending on a certain set of selection rules.

A typical EDSR transition is done between two uncoupled spin states. However, when two levels are involved in an avoided crossing, then driving the system through this anticrossing is described by the Landau-Zener dynamics instead. When the driving is periodic, the system accumulates the Stückelberg phase between the transitions and this leads to a constructive or destructive interference, depending on the specific parameters of a given system. The theory related to systems of this kind is described in a review article of Ref. [12].

Multiple harmonic generation in EDSR in an InAs nanowire double quantum dot was recently observed for conduction band electrons in double quantum dots [13]. The harmonics displays a remarkable detuning dependence: Near the interdot charge transition as many as eight harmonics were observed, while at large detunings only the fundamental spin resonance condition was detected. The transport dynamics of a periodically driven system, modeling the level structure of a two-electron double quantum dot, was studied theoretically [14,15]. It was shown that the observed multiphoton resonances, which are dominant near interdot charge transitions, are due to multilevel Landau-Zener-Stückelberg-Majorana interference. The main features observed in the experiments of Ref. [13] were replicated: multiphoton resonances up to eight photons, a robust odd-even dependence, and oscillations in the electric dipole spin-resonance signal as a function of energy-level detuning.

The Landau-Zener dynamic was used to study the possibility of manipulating the singlet-triplet (S-T+) avoided crossing that arises due to the hyperfine interactions in a system of two electrons in a double quantum dot in GaAs [16,17]. The results concern a two-electron Landau-Zener system with the spin-mixing singlet-triplet avoided crossing, resulting from the hyperfine interaction. In both works, the necessity of going beyond the simplest infinite-time Landau-Zener model is stressed out, and the finite-time Landau-Zener theory is employed. Moreover, the formulated master-equation formalism allowed one to study the impact of phonon-mediated hyperfine relaxation and charge-noise-induced dephasing on the evolution of the system [17]. In the corresponding experimental work [18], an all-electrical method for quantum control was presented that relies on electron-nuclear spin coupling and drives spin rotations on nanosecond time scales. Interference patterns were observed [18] in singlet-state occupation as a function of waiting time between consecutively sweeping the system back and forth through a singlet-triplet avoided crossing, due to phase accumulation, in agreement with the Landau-Zener theory.

In a recent work, a *p*-channel silicon metal-oxide-semiconductor field-effect transistor with a double dot in the channel, formed by a pair of defects or impurities, was studied [19]. A two-spin EDSR was realized experimentally, with the main line as well as additional few-photon lines visible. A suppression of the spin resonance was found in the vicinity of a singlet-triplet avoided crossing.

II. MOTIVATION

The EDSR manipulation scheme was realized for valence band holes in a quantum molecule created in a gated InSb nanowire [11]. The mentioned work employed the strong spin-orbit coupling of this material for the spin flipping and measured the transport through the system as a result of lifting the Pauli spin blockade.

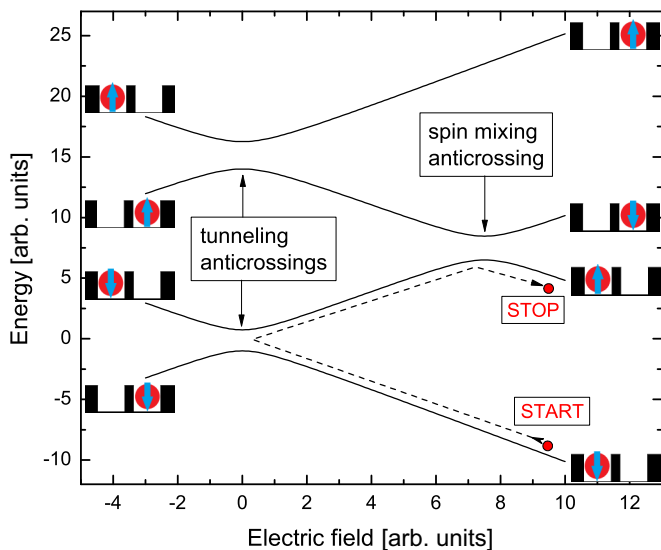


FIG. 1. An illustrative scheme of the transfer process idea. The spin-dependent energy-level structure is shown with the desired spin-flipping process utilizing two avoided crossings.

In this paper, we suggest a scheme for reversing the spin state of a single hole confined in two electrostatic quantum dots with tunneling coupling in a nanowire. The energy-level structure of the system is presented schematically in Fig. 1. First, by application of an external magnetic field along the axis of the nanowire, an energy shift between the opposite spin states, previously degenerated, is introduced—see the energy difference between two tunneling anticrossings on the left-hand side of Fig. 1. Second, we have taken advantage of an avoided crossing that involves the states localized in different dots with an opposing spin characteristic that appears in the spectrum—see the right-hand side of Fig. 1. Its appearance occurs due to the spin-orbit interaction and it is procured by the shift mentioned above. We propose that an electrical control signal can be applied that leads to a transition from the ground state, of the heavy-hole spin-down type, to the first excited state, of the heavy-hole spin-up type—see the dashed line leading from the “START” to “STOP” points in Fig. 1. Instead of using a long periodic signal, as is typically done in EDSR processes, the system will be driven through two anticrossings only a few times by a short cosine impulse.

The specifics of the impulse have been determined in our calculations and a high transition efficiency of about 0.99 was obtained by a detailed balancing of the impulse parameters. The process is one order of magnitude faster than the alternative EDSR approach, of a similar electric field amplitude, realized in the same system, which is especially important in the context of limited spin coherence time when performing spin operations.

III. THEORY

A. Geometry of the system

We consider a system of a single hole in a quantum molecule consisting of two quantum dots coupled vertically. The dots are made by applying an external electrostatic potential to an InSb quantum wire of a $\langle 111 \rangle$ zinc-blende crystal structure.

The nanowire is assumed to have a circular shape in the cross section and a radius of $R_{\text{dot}} = 50$ nm. The geometry of the system is similar to the one considered in Ref. [11].

We model a confinement potential of two vertically stacked quantum dots in the form of an infinite circular quantum well in the xy plane (corresponding to the cross section of the wire) and two finite quantum wells along the z axis (the growth axis of the wire). The zero of the energy scale is set to the degenerated top of the heavy- and light-hole bands outside the dots. The total potential is $\hat{U} = [V_{xy}(\rho) + V_z(z)]\mathbf{I}$, where \mathbf{I} is the unity matrix,

$$V_{xy}(\rho) = \begin{cases} 0, & \rho \leq R_{\text{dot}}, \\ \infty, & \rho > R_{\text{dot}}, \end{cases} \quad (1)$$

and

$$V_z(z) = V_0 [V_z^d(z + z_0) + V_z^d(z - z_0)],$$

$$V_z^d(z) = -\frac{e^{\frac{z}{4}} \left(1 + e^{\frac{H_d}{8}}\right)^2}{e^{\frac{z}{4}} + e^{\frac{z+H_d}{4}} + e^{\frac{4z+H_d}{8}} + e^{\frac{H_d}{8}}},$$

$$z_0 = \frac{1}{2}(H_b + H_d). \quad (2)$$

In the above equation, the $V_z^d(z + z_0)$ part corresponds to the shape of the confinement of one of the dots and the $V_z^d(z - z_0)$ part corresponds to the shape of the confinement of the other one. $V_0 = 50$ meV is the depth of the confinement. The $H_b = 11$ nm parameter describes the separation of the dots and $H_d = 40$ nm describes the width of the dots. The $V_z(z)$ potential is presented in Fig. 2(a) and the shape of the dots in Fig. 2(b).

The adopted potential defining the system is symmetric with respect to reversing the nanowire z axis. In any experimental realization, the potential for each dot would be slightly different. We have studied the impact of the asymmetry of the dots in Appendix E.

B. Kohn-Luttinger Hamiltonian

We work in the effective mass approximation. The kinetic energy of holes is calculated using the four-band Kohn-Luttinger Hamiltonian [20]. The Hamiltonian for $\langle 100 \rangle$ crystal orientation is given (in atomic units) by

$$\hat{T}_{100} = \frac{1}{2} \left(\gamma_1 + \frac{5}{2} \gamma_2 \right) k^2 \mathbf{I} - 2\gamma_2 (k_x^2 J_x + k_y^2 J_y + k_z^2 J_z) - 4\gamma_3 (k_x k_y J_{xy} + k_y k_z J_{yz} + k_z k_x J_{zx}), \quad (3)$$

where J_x, J_y, J_z are the spin matrices for spin $\frac{3}{2}$, $J_{ij} = \frac{1}{2}(J_i J_j + J_j J_i)$, $\gamma_1, \gamma_2, \gamma_3$ are the Luttinger parameters, and $k^2 = k_x^2 + k_y^2 + k_z^2$ [21,22]. To obtain the expression of the same Hamiltonian for $\langle 111 \rangle$ orientation, one should express the $(k_x, k_y, k_z)_{100}$ and $(J_x, J_y, J_z)_{100}$ vectors of the $\langle 100 \rangle$ orientation in the terms of $(k_x, k_y, k_z)_{111}$ and $(J_x, J_y, J_z)_{111}$ vectors of the $\langle 111 \rangle$ orientation, respectively (see Appendix A).

If written in the basis $(\text{HH}\uparrow, \text{LH}\downarrow, \text{LH}\uparrow, \text{HH}\downarrow) = (|\frac{3}{2}, +\frac{3}{2}\rangle, |\frac{3}{2}, -\frac{1}{2}\rangle, |\frac{3}{2}, +\frac{1}{2}\rangle, |\frac{3}{2}, -\frac{3}{2}\rangle)$ the Hamiltonian for

TABLE I. The operators used in the KL Hamiltonian definition.

| | |
|--|--|
| $\hat{P}_+ = \frac{(\gamma_1+\gamma_3)\hat{k}_x^2+(\gamma_1-2\gamma_3)\hat{k}_z^2}{2}$ | $\hat{P}_- = \frac{(\gamma_1-\gamma_3)\hat{k}_x^2+(\gamma_1+2\gamma_3)\hat{k}_z^2}{2}$ |
| $\hat{R}_s = -\frac{\sqrt{3}}{6}(\gamma_2+2\gamma_3)\hat{k}_-^2$ | $\hat{R}_{as} = \frac{\sqrt{6}}{3}(\gamma_2-\gamma_3)\hat{k}_+\hat{k}_z$ |
| $\hat{S}_s = \frac{\sqrt{3}}{3}(2\gamma_2+\gamma_3)\hat{k}_-\hat{k}_z$ | $\hat{S}_{as} = -\frac{\sqrt{6}}{6}(\gamma_2-\gamma_3)\hat{k}_+^2$ |
| $\hat{k}_- = \hat{k}_x - i\hat{k}_y$ | $\hat{k}_+ = \hat{k}_x + i\hat{k}_y$ |
| $\hat{k}_\pm^2 = \hat{k}_x^2 + \hat{k}_y^2$ | |

the (111) orientation has the following form,

$$\hat{T} = \begin{pmatrix} \hat{P}_+ & \hat{R}_s + \hat{R}_{as} & -\hat{S}_s - \hat{S}_{as} & 0 \\ \hat{R}_s^* + \hat{R}_{as}^* & \hat{P}_- & 0 & \hat{S}_s + \hat{S}_{as} \\ -\hat{S}_s^* - \hat{S}_{as}^* & 0 & \hat{P}_- & \hat{R}_s + \hat{R}_{as} \\ 0 & \hat{S}_s^* + \hat{S}_{as}^* & \hat{R}_s^* + \hat{R}_{as}^* & \hat{P}_+ \end{pmatrix}, \quad (4)$$

where the operators used in this definition are listed in Table I.

The Kohn-Luttinger Hamiltonian can be divided into two parts,

$$\begin{aligned} \hat{T} &= \hat{T}_s + \hat{T}_{as}, \\ \hat{T}_s &= \begin{pmatrix} \hat{P}_+ & \hat{R}_s & -\hat{S}_s & 0 \\ \hat{R}_s^* & \hat{P}_- & 0 & \hat{S}_s \\ -\hat{S}_s^* & 0 & \hat{P}_- & \hat{R}_s \\ 0 & \hat{S}_s^* & \hat{R}_s^* & \hat{P}_+ \end{pmatrix}, \\ \hat{T}_{as} &= \begin{pmatrix} 0 & \hat{R}_{as} & -\hat{S}_{as} & 0 \\ \hat{R}_{as}^* & 0 & 0 & \hat{S}_{as} \\ -\hat{S}_{as}^* & 0 & 0 & \hat{R}_{as} \\ 0 & \hat{S}_{as}^* & \hat{R}_{as}^* & 0 \end{pmatrix}. \end{aligned} \quad (5)$$

The \hat{T}_s part is axially symmetric and hence its eigenstates have defined z components of total angular momentum $J_z = J_z^{\text{Bl}} + J_z^{\text{en}}$, which is the sum of Bloch J_z^{Bl} and envelope J_z^{en} z components. For this reason, the computation of the system described by \hat{T}_s is much easier as the process for each one of the J_z subspaces can be done separately. The envelope

eigenfunctions of \hat{T}_s are four-dimensional vector functions,

$$\Psi_{(J_z, m)}^{\text{ax}}(\vec{r}_h) = \begin{pmatrix} \xi_{J_h}^{\text{HH}\uparrow} e^{i(J_z-3/2)\phi} \\ \xi_{J_h}^{\text{LH}\downarrow} e^{i(J_z+1/2)\phi} \\ \xi_{J_h}^{\text{LH}\uparrow} e^{i(J_z-1/2)\phi} \\ \xi_{J_h}^{\text{HH}\downarrow} e^{i(J_z+3/2)\phi} \end{pmatrix}. \quad (6)$$

Moreover, the non-axially-symmetric part \hat{T}_{as} is relatively small: The constant in \hat{R}_s is about 14 times greater than the one in \hat{R}_{as} , and the constant in \hat{S}_s about 54 times greater than the one in \hat{S}_{as} .

The diagonal terms of the $\hat{T}_s + \hat{U}$ Hamiltonian,

$$\begin{aligned} \hat{H}_{\text{HH}\uparrow} &= \hat{H}_{\text{HH}\downarrow} = \hat{P}_+ + [V_{xy}(\rho) + V_z(z)], \\ \hat{H}_{\text{LH}\uparrow} &= \hat{H}_{\text{LH}\downarrow} = \hat{P}_- + [V_{xy}(\rho) + V_z(z)], \end{aligned} \quad (7)$$

have the corresponding envelope eigenfunctions,

$$\begin{aligned} \psi_{k, J_z^{\text{en}}, n}^{\text{HH}}(\vec{r}_h) &= e^{iJ_z^{\text{en}}\phi} \chi_{J_z^{\text{en}}} \left(\frac{\chi_0(k, J_z^{\text{en}})\rho}{R} \right) Z_n^{\text{HH}}(z), \\ \psi_{k, J_z^{\text{en}}, n}^{\text{LH}}(\vec{r}_h) &= e^{iJ_z^{\text{en}}\phi} \chi_{J_z^{\text{en}}} \left(\frac{\chi_0(k, J_z^{\text{en}})\rho}{R} \right) Z_n^{\text{LH}}(z), \end{aligned} \quad (8)$$

where $\chi_{J_z^{\text{en}}}$ is a Bessel function of the first kind of (J_z^{en}) th order and $\chi_0(k, J_z^{\text{en}})$ is the k th zero of that function. The n quantum numbers order the $Z_n^{\text{HH}}(z)$ functions by ascending energy and (separately) order the $Z_n^{\text{LH}}(z)$ functions in the same way.

Finally, the Hamiltonian for the axially symmetric static system is

$$\hat{H}_s = \hat{T}_s + \hat{U} + \hat{H}_{B_z} + \hat{H}_{F_z}, \quad (9)$$

where \hat{H}_{B_z} and \hat{H}_{F_z} are the magnetic field and electric field Hamiltonians (as defined below), respectively. As the last two terms do not mix states with different J_z quantum numbers, the eigenfunctions of Eq. (9) also have the form presented in Eq. (6).

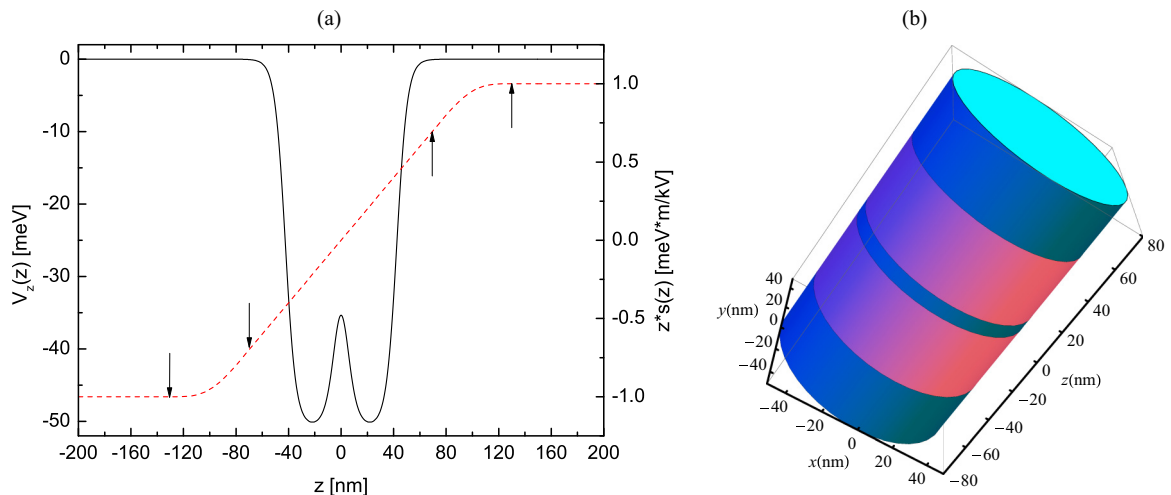


FIG. 2. (a) Solid line, left axis: The confinement potential along the z axis. Dashed line, right axis: The $z s(z)$ shape function of the electric field F_z . The arrows correspond to the “sewing” points in Eq. (10). (b) Shape of the dots. The z boundary is shown for $V_z(z) = \frac{V_0}{2}$.

C. Electric and magnetic fields

The Hamiltonian of the external electric field, applied along the growth z axis, in atomic units, has the form of

$$\hat{H}_{F_z} = F_z z s(z), \quad s(z) = \begin{cases} 1, & |z| \leq 70 \text{ nm}, \\ \frac{100}{|z|}, & |z| \geq 130 \text{ nm}, \\ |s_p(z)|, & 70 \text{ nm} \leq |z| \leq 130 \text{ nm}, \end{cases} \quad (10)$$

where F_z is the electric field amplitude and $s(z)$ is the shape function used to allow the electric field dependence (linear in z) to be felt only in the dot region [see Fig. 2(a)]. The motivation for using the shape function $s(z)$ is for numerical purposes—to avoid an additional artificial bonding center appearing near the end of the computational box. The $s(z)$ has such a character that it simulates an electric field that (i) is homogeneous in the area of the dots, (ii) is continuous everywhere up to the second derivative, and (iii) decreases as $\frac{1}{|z|}$ in area far from the system. $s_p(z)$ is the simplest polynomial that meets the continuity assumptions [23].

The Hamiltonian of the homogeneous magnetic field $\vec{B} = (0, 0, B_z)$, in atomic units, is given by

$$\begin{aligned} (\hat{H}_{B_z})_{11} &= \frac{B_z}{2} \left[(\gamma_1 + \gamma_3) \left(J_z - \frac{3}{2} \right) + \frac{3\kappa}{2} \right], \\ (\hat{H}_{B_z})_{22} &= \frac{B_z}{2} \left[(\gamma_1 - \gamma_3) \left(J_z + \frac{1}{2} \right) - \frac{\kappa}{2} \right], \\ (\hat{H}_{B_z})_{33} &= \frac{B_z}{2} \left[(\gamma_1 - \gamma_3) \left(J_z - \frac{1}{2} \right) + \frac{\kappa}{2} \right], \\ (\hat{H}_{B_z})_{44} &= \frac{B_z}{2} \left[(\gamma_1 + \gamma_3) \left(J_z + \frac{3}{2} \right) - \frac{3\kappa}{2} \right], \\ (\hat{H}_{B_z})_{ij} &= 0, \quad i \neq j, \end{aligned} \quad (11)$$

where κ is the g -factor for heavy and light holes in the system. This is a model that was used in Ref. [24], but with two changes: (i) The inverted effective mass values for heavy holes in the xy plane $\gamma_1 + \gamma_2$ and the light holes one $\gamma_1 - \gamma_2$ for (100) orientation were substituted by analogous values for the (111) system (i.e., $\gamma_1 + \gamma_3$ and $\gamma_1 - \gamma_3$, respectively) and (ii) we omit the terms proportional to B_z^2 as they are very small for the range of magnetic field that was considered [25]. The g -factor for bulk InSb is equal to 15.6, but in a system of this type the value is significantly quenched, i.e., $\kappa \in (0, 4)$ [11]. The Landé value, which does not take into account the influence of remote bands, is $4/3$. We decided to adopt a middle value of $\kappa = 2.0$.

D. Dresselhaus Hamiltonian

In order to account for the mixing of the states with different spins, the Dresselhaus Hamiltonian was included. In the case of (100) crystal orientation it has the form of

$$\begin{aligned} \hat{H}_D^{100} &= \frac{2}{\sqrt{3}} C_k \{ k_x \{ J_x, J_y^2 - J_z^2 \} + \text{c.p.} \} \\ &+ b_{41} \{ \{ k_x, k_y^2 - k_z^2 \} J_x + \text{c.p.} \} \\ &+ b_{42} \{ \{ k_x, k_y^2 - k_z^2 \} J_x^3 + \text{c.p.} \} \\ &+ b_{51} \{ \{ k_x, k_y^2 + k_z^2 \} \{ J_x, J_y^2 - J_z^2 \} + \text{c.p.} \} \\ &+ b_{52} \{ k_x^3 \{ J_x, J_y^2 - J_z^2 \} + \text{c.p.} \}, \end{aligned} \quad (12)$$

TABLE II. The material constants used for Dresselhaus Hamiltonian definition.

| | |
|--|--|
| $c_1 = \frac{12b_{41}+23b_{42}}{16\sqrt{6}}$ | $c_2 = -\frac{4b_{41}+9b_{42}+4(b_{51}+b_{52})}{16}$ |
| $c_3 = \frac{4b_{41}+9b_{42}-4b_{51}+4b_{52}}{8\sqrt{2}}$ | $c_4 = \frac{4b_{41}+9b_{42}-2b_{52}}{4}$ |
| $c_5 = \frac{-b_{42}+b_{51}+b_{52}}{4\sqrt{2}}$ | $c_6 = \frac{b_{42}+b_{51}-b_{52}}{4\sqrt{3}}$ |
| $c_7 = \frac{2b_{42}+b_{52}}{2\sqrt{2}}$ | $c_8 = \frac{b_{42}-b_{51}+b_{52}}{4\sqrt{3}}$ |
| $c_9 = \frac{2b_{51}+b_{52}}{\sqrt{6}}$ | $c_{10} = \frac{-4b_{41}-7b_{42}+6(b_{51}+b_{52})}{8\sqrt{3}}$ |
| $c_{11} = \frac{4b_{41}+7b_{42}+6b_{51}-6b_{52}}{4\sqrt{6}}$ | $c_{12} = \frac{4b_{41}+7b_{42}+3b_{52}}{2\sqrt{3}}$ |
| $c_{13} = \sqrt{\frac{3}{2}} b_{52}$ | $a = \frac{4b_{41}+13b_{42}}{12b_{41}+23b_{42}}$ |

where C_k , b_{41} , b_{42} , b_{51} , b_{52} are material parameters, $\{A, B\} = \frac{1}{2}(AB + BA)$ and c.p. stands for cyclic permutations of the preceding terms [26,27]. The procedure for obtaining the Hamiltonian for (111) orientation is the same as for the Kohn-Luttinger Hamiltonian (see Appendix A). It leads to the following result,

$$\hat{H}_D = \begin{pmatrix} \hat{O}_1 & \hat{O}_3 & \hat{O}_2 & \hat{O}_4 \\ \hat{O}_3^+ & -a\hat{O}_1 & \hat{O}_5 & \hat{O}_2 \\ \hat{O}_2^+ & \hat{O}_5^+ & a\hat{O}_1 & -\hat{O}_3 \\ \hat{O}_4^+ & \hat{O}_2^+ & -\hat{O}_3^+ & -\hat{O}_1 \end{pmatrix}, \quad (13)$$

where the element operators are defined as follows,

$$\begin{aligned} \hat{O}_1 &= -c_1(i\hat{k}_-)^3 + c_1(i\hat{k}_+)^3, \\ \hat{O}_2 &= -\frac{C_k}{\sqrt{3}}(i\hat{k}_-) + c_2\hat{k}_\perp^2(i\hat{k}_-) - ic_3\hat{k}_z(i\hat{k}_+)^2 + c_4\hat{k}_z^2(i\hat{k}_-), \\ \hat{O}_3 &= \frac{C_k}{\sqrt{6}}(i\hat{k}_+) + c_5\hat{k}_\perp^2(i\hat{k}_+) - i\sqrt{3}c_6\hat{k}_z(i\hat{k}_-)^2, \\ \hat{O}_4 &= c_6(i\hat{k}_-)^3 - c_8(i\hat{k}_+)^3 - ic_{13}\hat{k}_z\hat{k}_\perp^2 - i\sqrt{2}C_k\hat{k}_z - ic_9\hat{k}_z^3, \\ \hat{O}_5 &= -C_k(i\hat{k}_+) - c_{10}\hat{k}_\perp^2(i\hat{k}_+) + ic_{11}\hat{k}_z(i\hat{k}_-)^2 - c_{12}\hat{k}_z^2(i\hat{k}_+), \end{aligned} \quad (14)$$

where constants a and c_1 - c_{13} are defined in the terms of b_{41} , b_{42} , b_{51} , and b_{52} (see Table II). Please note that if the angular dependencies of $|L\rangle$ and $|R\rangle$ states are $e^{iL\phi}$ and $e^{iR\phi}$, respectively, then the $\langle L|\hat{k}_+|R\rangle$ matrix element is nonzero only for $l_R = l_L + 1$, the $\langle L|\hat{k}_+|R\rangle$ matrix element is nonzero only for $l_R = l_L - 1$, and the $\langle L|\hat{k}_\perp^2|R\rangle$ and the $\langle L|\hat{k}_z|R\rangle$ matrix elements are nonzero only for $l_R = l_L$. This leads to a significant simplification of the Hamiltonian (see Appendix B).

E. Computational method

Our computational method consists of several separable steps. At the beginning, the one-band hole Hamiltonian eigenequations (7) are solved. The $Z_n^{\text{HH}}(z)$ and $Z_n^{\text{LH}}(z)$ functions in Eq. (8) are determined by direct diagonalization on one-dimensional mesh with a mesh spacing $\Delta_z = 0.5$ nm and computation box of $z \in (-200 \text{ nm}, 200 \text{ nm})$. Afterwards, the $\Psi_{(J_z, m)}^{\text{ax}}(\vec{r})$ eigenfunctions of the axially symmetric Hamiltonian Eq. (9) are obtained in a base constructed by taking functions of the type as in formula (8) with $k \in \{1, 8\}$, $n \in \{1, 32\}$,

and $J_z \in \{-\frac{13}{2}, \dots, \frac{13}{2}\}$. As it was mentioned before, each J_z defines a separable subspace and the m quantum number sorts the eigenfunctions of each subspace in the order of ascending energy.

The next step is to include the nonaxial part into the calculation. This part consists of the small nonaxial terms in the Kohn-Luttinger Hamiltonian and of the Dresselhaus Hamiltonian,

$$\hat{H}_{as} = \hat{T}_{as} + \hat{H}_D. \quad (15)$$

This operation is made in a basis consisting of a selected set of lowest-lying \hat{H}_s eigenstates,

$$\Lambda_j(\vec{r}) = \sum_{(J_z, m) \in \Lambda_{\text{basis}}} \lambda_{j, (J_z, m)} \Psi_{(J_z, m)}^{\text{ax}}(\vec{r}), \quad (16)$$

where Λ_{basis} is the basis for the non-axially-symmetric calculation and $\lambda_{j, (J_z, m)}$ is the projection of the j th nonaxial state onto an individual (J_z, m) basis state.

F. Evolution

The total Hamiltonian for the time-dependent calculation is

$$\hat{H}_{\text{ev}}(t) = \hat{T}_s + \hat{U} + \hat{H}_{B_z} + \hat{H}_{as} + \hat{H}_{F_z}(t), \quad (17)$$

where $\hat{H}_{F_z}(t) = F_z(t)z\mathcal{S}(z)$ is the time-dependent part. The function $F_z(t)$ can be, in general, arbitrary. The specifics of such $F_z(t)$ that manage to accomplish the desired spin operation on the system remain to be found in the course of our study.

The evolution simulation of the system is done with the Runge-Kutta method of the fourth order with a time step of $\Delta_t = 0.2$ fs. The basis for the evolution is the set of states obtained in the non-axially-symmetric calculation, without the external electric field,

$$\Phi(\vec{r}, t) = \sum_{j \in \Phi_{\text{basis}}} d_j(t) \Lambda_j(\vec{r}; F_z = 0), \quad (18)$$

where Φ_{basis} is the evolution basis and d_j is the projection of the time-dependent state onto an individual j th basis state (in order of ascending energy). The specific algorithm for the evolution of d_j projections is described in Appendix C.

Please note that all results for the evolution are presented in a *local* F_z basis (also known as instantaneous basis),

$$\Phi(\vec{r}, t) = \sum_j d_j^l(t) \Lambda_j(\vec{r}), \quad (19)$$

and not in the $F_z = 0$ basis [see Eq. (18)], for ease of interpretation. The projections $d_j(t)$, obtained as have been explained above, are recalculated to represent the projections as if the levels $\Lambda_j(\vec{r})$ at each given F_z were the basis states instead of the $\Lambda_j(\vec{r}; F_z = 0)$ states,

$$d_j^l(t) = \sum_i d_i(t) \langle \Lambda_j | \Lambda_i(F_z = 0) \rangle. \quad (20)$$

This way, one can refer to these projections as corresponding to the instantaneous basis in each given moment of the evolution.

G. Parametrization

The values of material constants for the Dresselhaus Hamiltonian, i.e.,

$$\begin{aligned} C_k &= -0.82 \text{ meV nm}, & b_{41} &= -934.8 \text{ meV nm}^3, \\ b_{42} &= 41.73 \text{ meV nm}^3, & b_{51} &= 13.91 \text{ meV nm}^3, \\ b_{52} &= -27.82 \text{ meV nm}^3, \end{aligned}$$

are taken from Ref. [27]. All the other material parameters were taken from the work of Vurgaftman *et al.* [28]. Luttinger parameters for InSb are $\gamma_1 = 34.8$, $\gamma_2 = 15.5$, and $\gamma_3 = 16.5$.

IV. RESULTS

A. Time-independent system

We begin by studying the energy spectrum with a static electric field F_z applied. The energy spectrum of the hole system for the axially symmetric Hamiltonian H_s [see Eq. (9)] for $B_z = 150$ mT is presented in Fig. 3(a). The set of levels with the lowest energies has the following elements: $(J_z = -\frac{3}{2}, m = 1)$, $(J_z = -\frac{3}{2}, m = 2)$, $(J_z = \frac{3}{2}, m = 1)$, and $(J_z = \frac{3}{2}, m = 2)$. This set of levels is separated energetically from the next ones for any F_z in the considered range by about 0.53 meV. The characteristics of the four lowest-lying \hat{H}_s eigenstates are given in Table III. In every case, the dominating valence band is the one with the lowest $|J_z^{\text{en}}|$ value (that equals 0 for the first four levels), and, in each case, it is one of the heavy-hole bands.

The main two features of this spectrum are the two avoided crossings: the one of the two $J_z = -\frac{3}{2}$ levels [marked as A in Fig. 3(a)] and the one of the two $J_z = \frac{3}{2}$ levels [marked as B in Fig. 3(a)]. The mentioned avoided crossings occur due to the tunneling coupling between the dots. At $F_z = 0$ the confinement potential of the system is symmetric in respect to $z = 0$, hence the eigenfunctions are equally distributed between both dots. For $F_z \gg 0$, away from the crossing, the hole is localized in the energetically preferable $z < 0$ dot in the ground level of each J_z subspace (i.e., levels with $m = 1$) and in the energetically unpreferable $z > 0$ dot in the excited levels (i.e., levels with $m = 2$). The situation is reversed for $F_z \ll 0$.

In the case of the non-axially-symmetric calculation, due to computational constraints, we are interested in the lowest-lying states only. Due to an energy separation of about 0.53 meV, the first four energy levels, shown in Fig. 3(a), create a natural basis for this calculation. Thus we define the basis Λ_{basis} in Eq. (16) as the set of levels listed in Table III.

TABLE III. The characteristics of the four lowest-lying \hat{H}_s eigenstates that make up the variational base Λ_{basis} .

| Level | Dominating valence band | Set of J_z^{en} values |
|-------------------------------|-------------------------|---------------------------------|
| $(J_z = -\frac{3}{2}, m = 1)$ | HH↓ | $(-3, -1, -2, 0)$ |
| $(J_z = -\frac{3}{2}, m = 2)$ | HH↓ | $(-3, -1, -2, 0)$ |
| $(J_z = \frac{3}{2}, m = 1)$ | HH↑ | $(0, 2, 1, 3)$ |
| $(J_z = \frac{3}{2}, m = 2)$ | HH↑ | $(0, 2, 1, 3)$ |

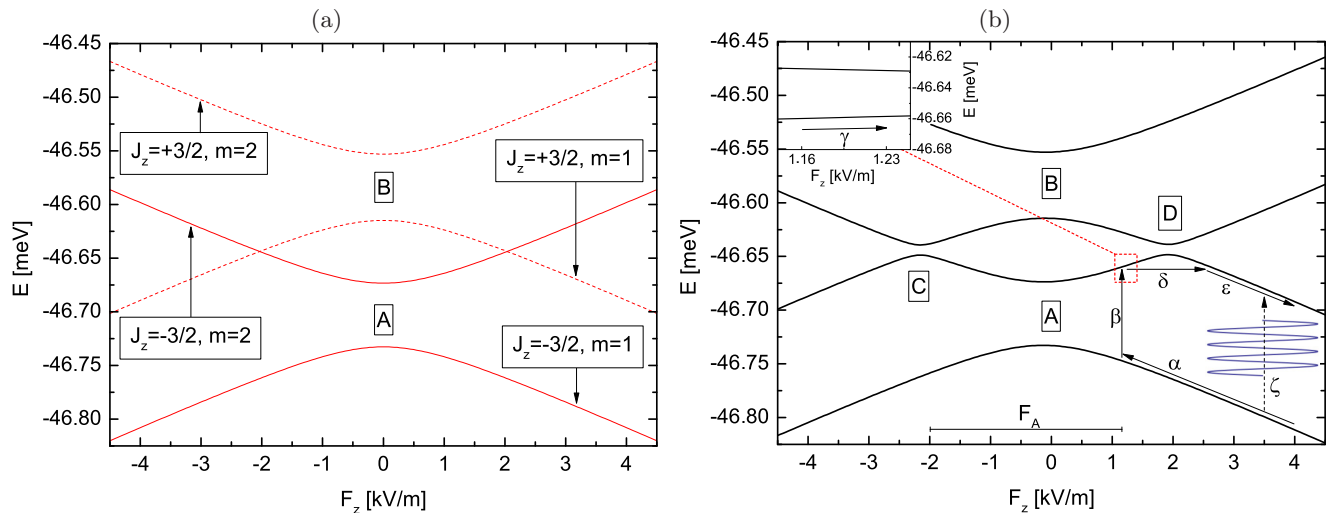


FIG. 3. (a) Hole energy spectrum of the axially symmetric system. (b) Hole energy spectrum of the system with non-axially-symmetric inclusions and the scheme of the hole transfer. Arrows indicate the successive steps of the process. F_A is the field range used for the Landau-Zener transfer in the β step. The dashed ζ arrow denotes an alternative EDSR approach (see Sec. IV C). The inset is a fragment of the spectrum in magnification.

The hole energy spectrum for the total Hamiltonian is presented in Fig. 3(b). In comparison to the axial one [see Fig. 3(a)], the only important difference is the formation of two additional smaller avoided crossings, marked as C and D in Fig. 3(b). These anticrossings correspond to the mixing of the $(J_z = -\frac{3}{2}, m = 1)$ state, that is, the spin-down state, and the $(J_z = \frac{3}{2}, m = 1)$ state, that is, the spin-up one. Apart from that, the energy shifts are very small, and the spectrum in Fig. 3(b) is nearly the same as the one in Fig. 3(a).

The one-band densities, integrated over the ϕ coordinate, are defined as follows,

$$P_{j,k}(\rho, z) = \rho \int_0^{2\pi} \Lambda_j^*(\rho, \phi, z) \mathbf{I}_k \Lambda_j(\rho, \phi, z) d\phi, \quad (21)$$

$$\mathbf{I}_k = \begin{pmatrix} \delta_{1,k} & 0 & 0 & 0 \\ 0 & \delta_{2,k} & 0 & 0 \\ 0 & 0 & \delta_{3,k} & 0 \\ 0 & 0 & 0 & \delta_{4,k} \end{pmatrix},$$

where $\delta_{i,k}$ is the Kronecker delta. They describe, for $k \in \{1, 4\}$, the partial spatial densities with respect to each of the Bloch bands, i.e., $(\text{HH}\uparrow, \text{LH}\downarrow, \text{LH}\uparrow, \text{HH}\downarrow)$. They are shown for $F_z = 4$ kV/m: $P_{1,k}$ in Fig. 4(a) for the ground state, the intended initial state of the evolution, and $P_{2,k}$ in Fig. 4(b) for the first excited level, the intended final state of the evolution, respectively. The ground state of the hole is localized in the $z < 0$ dot and is strongly dominated by the $\text{HH}\downarrow$ band. The first excited state is localized in the same dot and is strongly dominated by the $\text{HH}\uparrow$ band. This corresponds to our idea to flip the spin of a hole by transferring it from the ground state to the first excited level. This would result in reversing the state from being $\text{HH}\downarrow$ dominated to being $\text{HH}\uparrow$ dominated, while remaining in the same $z < 0$ dot. In order to do so, we plan to employ the Landau-Zener transitions of A and D avoided crossings [see Fig. 3(b)].

B. Evolution

The idea of the spin flip is presented in Fig. 3(b). The initial state of the simulation is the time-independent ground state at $F_z = 4$ kV/m and the intended final state is the time-independent first excited state at the same electric field. The transfer is planned to be made in five steps. It should start with tuning the electric field to the $F_z > 0$ side of the larger avoided crossing in such a way that the time-dependent state would remain equal to the time-independent ground level [arrow α in Fig. 3(b)]. The second step consists of using this anticrossing to transfer the time-dependent hole state to the first excited level at the same electric field [arrow β in Fig. 3(b)]. The third stage is

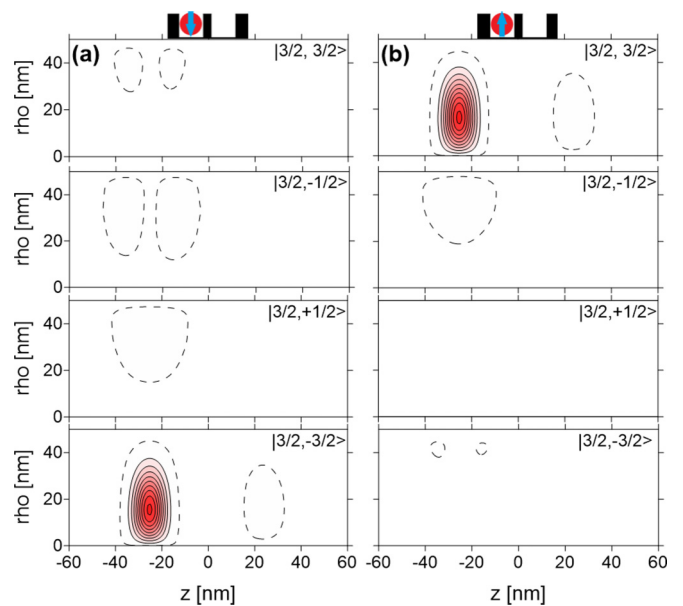


FIG. 4. The hole one-band densities integrated over the ϕ coordinate, for $F_z = 4$ kV/m: (a) $P_{1,k}(\rho, z)$ for the ground state, and (b) $P_{2,k}(\rho, z)$ for the first excited level.

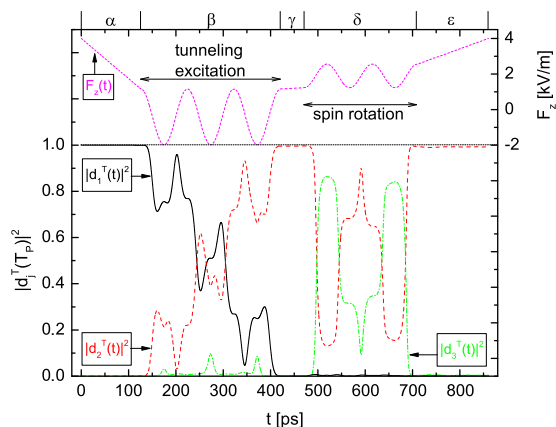


FIG. 5. The evolution process for the complete transition. Upper part, right axis: The driving field $F_z(t)$ function. Lower part, left axis: The $|d_j^T(t)|^2$ projections for the time-dependent state $\Phi(\vec{r}, t)$ on the j th time-independent state $\Lambda_j(\vec{r})$, respectively. For $j = 4$ the projection is not shown as it is negligible at every moment of the evolution.

the drive of the hole from the tunneling-generated anticrossing to the *lower* F_z side of the smaller spin-mixing one [arrow γ in the inset of Fig. 3(b)]. After that, the hole state should be transferred across the smaller avoided crossing without the *leak* of the time-dependent state to another time-independent level [arrow δ in Fig. 3(b)]. It is here that the spin flip takes place. The final step is the drive of the system to $F_z = 4$ kV/m [arrow ϵ in Fig. 3(b)].

Each of the $\{\alpha, \beta, \gamma, \delta, \epsilon\}$ stages was optimized separately for transfer efficiency in terms of relevant parameters (see Appendix D) and the total $F_z(t)$ driving impulse was constructed by joining all the parts together. The evolution of the total transfer is presented in Fig. 5. The initial state is equal to the time-independent ground state $\Psi_1(\vec{r})$, that is, $d_1(0) = 1$. After the evolution, the evolving state ends in the first excited state $\Psi_2(\vec{r})$ with $|d_2(T_P)|^2 > 0.99$. This means that the system started and ended evolution in the same electric field. Both the initial and the final states are localized in the same dot. However, the system started evolution in a state dominated by the $\text{HH}\downarrow$ spin state and it ended it in a state dominated by the opposite $\text{HH}\uparrow$ spin state. This proposition of the process that reverses the spin state of the hole is the main result of this work.

C. Comparison with the EDSR of uncoupled levels

The Landau-Zener (LZ) type of spin flip is an alternative for the EDSR one. In the latter case, the levels involved in the transition are not engaged in an avoided crossing. In order to make a comparison between these two mechanisms, the transition ζ in Fig. 3(b) was calculated. The frequency of the driving signal,

$$F_z(t) = F_o + A \cos(\omega_c t), \quad (22)$$

is tuned to resonance with the energy difference between the final and the initial level, $\omega_c = E_f - E_i = 2\pi \times 28.8$ GHz for the offset $F_o = 3.5$ kV/m. The amplitude of the EDSR signal is $A = 0.95$ kV/m. The results are presented in Fig. 6. The evolving state starts in the ground state of the time-independent system and then typical Rabi oscillations begin. The evolving

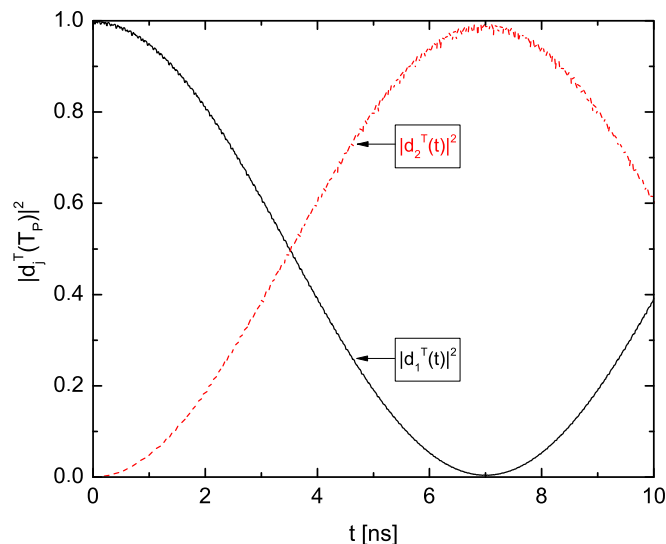


FIG. 6. The evolution process for the EDSR of uncoupled levels. The $|d_j(t)|^2$ projections for the time-dependent state $\Phi(\vec{r}, t)$ on the j th time-independent state $\Lambda_j(\vec{r})$, respectively. For $j \in \{3, 4\}$ the projections are not shown as they are negligible at every moment of the evolution.

state occupies the first excited state after $t \sim 7$ ns, which corresponds to about 200 periods of the F_z signal function. Please note that this time is about one order of magnitude larger than the time of the total evolution for the $\{\alpha, \beta, \gamma, \delta, \epsilon\}$ scheme. In general, increasing the driving amplitude A would decrease the time of the EDSR transition. However, we wanted to compare the EDSR and LZ approaches with the amplitudes of comparable orders of magnitude.

Moreover, there are two limits to increasing the driving field amplitude in the EDSR process: (i) It can cause the state to traverse the avoided crossings, therefore making the transition an LZ-like one and (ii) the EDSR Rabi oscillations are themselves a perturbation theory result and occur only if the amplitude of the driving is small in comparison to the energy difference between the involved levels.

V. NOISE

A. The models of the noise

The evolution simulation assumes total control of the driving electric field $F_z(t)$. In an experiment, such precise control is impossible. The impact of the *power-law noise* on the effectiveness of the transfer is studied by the implementation of a simple random telegraph noise model (RTN), as described in Ref. [29]. According to the model, the actual time dependence of the electric field is given by

$$F_z^e(t) = F_z(t) + F_N G_i(t, f_c), \quad (23)$$

where $F_z(t)$ is the nondistorted electric field drive, F_N is the jump amplitude of RTN,

$$G_i(t, f_c) = C_{\text{sgn}}(-1)^{\sum_j \Theta(t-t_{i,j})} \quad (24)$$

is the electric distortion of the RTN, Θ stands for the Heaviside step function, the sign of the first jump C_{sgn} is determined

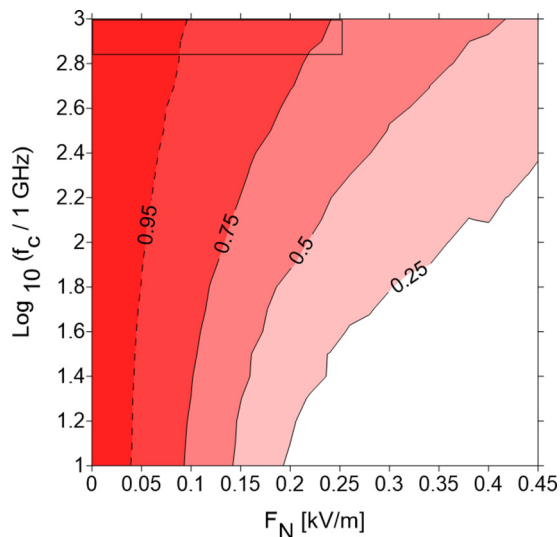


FIG. 7. The final $|d_2|^2$ projection for the RTN F_z noise simulation (the fast-variable noise regime). F_N is the amplitude of the noise and f_c is the characteristic frequency of the noise. The square in the upper left-hand corner marks the region where an analog of the motional narrowing occurs (see Appendix F).

randomly, and the time of the j th jump is defined as follows,

$$t_{i,j} = -\frac{1}{f_c} \sum_{n=1}^j \ln p_{i,n}. \quad (25)$$

In Eqs. (24) and (25) the i variable is the current iteration of random generation of a set of $p_{i,n}$ numbers from a uniform distribution over a $[0, 1]$ range. The characteristic frequency f_c is related to the average number of jumps occurring during the evolution time T_P ,

$$N_{\text{avg}} = T_P f_c. \quad (26)$$

It was shown that this model simulates the *power-law* noise well for a sufficiently high amount of jumps per one evolution ($f_c > 1$ GHz) [29]. On the opposite end of the scale, where the frequency of the noise change is low, e.g., if 90% of cases have no jumps ($f_c < 100$ MHz), a different model was adopted. The little variability in the noise signal during the evolution can be simulated by adopting a static shift in the electric field,

$$F_z^e(t) = F_z(t) \pm F_N, \quad (27)$$

where the sign of the shift is determined randomly.

B. The noise simulation

The results for the RTN noise model are presented in Fig. 7. The final efficiency was averaged over 1000 simulations for each pair of F_N and f_c values. Keeping the transfer efficiency equal, an increase in f_c leads to an increase in F_N . The mechanism of the observed effect is very similar to the one responsible for the motional narrowing effect in magnetic resonance (see, e.g., Ref. [30], pp. 212 and 213, and Appendix F). If the noise changes very quickly, then the system does not adapt to each individual shift value. The mean value of the noise shift is equal to zero, and so the overall effect of

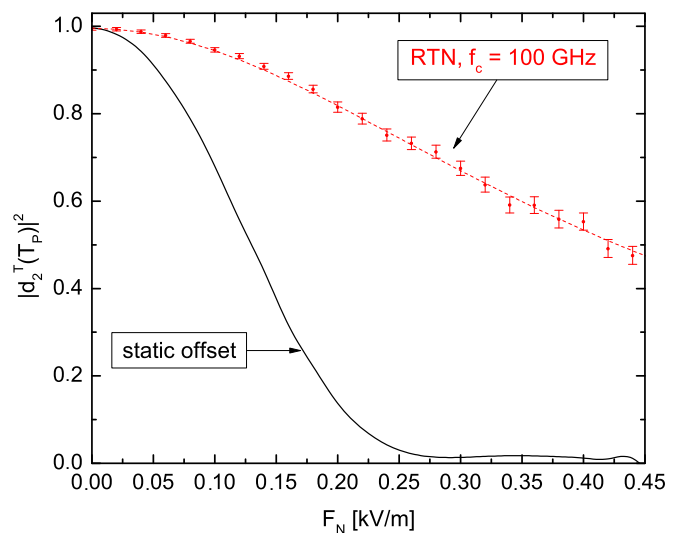


FIG. 8. The final $|d_2|^2$ projection for the static F_z offset (the slowly variable noise regime) (solid curve). The results for the maximal f_c considered in the RTN model are shown for comparison. The points are simulation data and the dotted line is a $1/(1 + cF_N^2)$ function fitted to the data.

the noise is diminished in comparison to the noise with lower f_c .

The results for the static offset are presented in Fig. 8. The value of the final projection was averaged over both possible signs of F_N . The effectiveness of the operation is nearly one for $F_N = 0$ and it drops to nearly zero as F_N increases. The condition for high fidelity $|d_2(T_P)|^2 > 0.9$ is in approximation $F_N < 0.05$ kV/m, and if $F_N > 0.13$ kV/m, then the probability of a successful operation is less than a half. These relations may be seen as estimates for the necessary conditions of an electric field control in any experimental realization of the presented scheme.

The imperfections in the F_z control process can be intuitively divided into two categories. The first one can be thought of, in a simplified way, as a systematic error type: Instead of the desired F_1 value, the system is tuned to $F_1 + \Delta$ at a given time and the *lifetime* of the Δ error value is large. The second type consists of errors constantly oscillating around the correct F_1 value (i.e., RTN model). We have shown that the first type of error, the static one, is more destructive to the described process than the second one. Thus the experimental setup used for the realization of the proposed scheme should especially minimize the systematic kind of F_z control error.

VI. DISCUSSION

The values of the parameters of any given realization of the quantum dot system are not perfectly known *a priori*. This relates to the exact size and geometry of the dots, the confining potential, the precise value of the g -factor, among others.

The energy spectrum depends on the following geometric and electrostatic parameters of the system: (i) depth of the binding potential, (ii) width of the barrier between the dots, (iii) size of the dots, and (iv) magnetic field intensity. Isolated parameters cannot be addressed separately. For example, for a given depth of potential, and a given barrier between the dots, some optimal width of the dots and value of the magnetic

field can be found. Unfortunately, as the dependence is highly nonlinear, there is no “rule of thumb” or simple formula. The suitable subspace of parameter values (potential, barrier, size of the dots, magnetic field) to obtain a suitable spectrum needs to be found numerically, if necessary. But because it is an extremely computationally demanding task (a nonlinear system with at least four degrees of freedom), it could be as well the subject of a separate study and we consider it outside the scope of this work.

Fortunately, the presented scheme is, on a general level, adaptive to the specifics of a given system. The only necessary condition is that the four lowest-lying eigenstates of a system need to be qualitatively similar to the ones presented in Fig. 3(b) for some magnetic field B_z and some electric field F_z range. That is, the two avoided crossings used for the transitions need to be present in the energy spectrum. Unfortunately, the efficiency of the whole process is strongly dependent on the specifics of the driving impulse, and these specifics depend in turn on the details of the previously mentioned parameters of the system. Thus, for a practical realization of this idea, it is necessary to study a given system experimentally in order to establish reliable estimates of the parameters. This is especially true in the case of the characteristic energy of the avoided crossing C in Fig. 3(b). Any imperfections in the axial symmetry of the nanowire shape as well as the piezoelectric effects (also breaking this symmetry) will contribute to the mixing of the states with different J_z values. In practice, it would be most efficient to take the approach of Ref. [14], i.e., to treat the anticrossing energy as a fittable parameter and try to deduce its value from experimental data. After that, one can employ the presented $\{\alpha, \beta, \gamma, \delta, \epsilon\}$ scheme and optimize each of the steps and join them together, as has been presented above.

The Kohn-Luttinger Hamiltonian allows one to obtain the hole energy spectrum, which is unknown *a priori*. In the results there are four energy-separated levels of such a spin structure that enable the realization of the spin-flip idea and create the basis for further steps of the calculation. The Dresselhaus Hamiltonian enables one to take into account the mixing of the opposite spin states. In order for the spin operation to be possible, the order of magnitude of the anticrossing energy, strongly dependent on the mixing on the valence bands, must be adequate. Thus we consider our model to be the minimal one for this work.

Please note that there are analytically integrable models for at least four-level Landau-Zener systems. They rely on the typical Landau-Zener assumptions, that is, (i) the evolution is done from $t = -\infty$ to $t = +\infty$, and (ii) the time derivative of the instantaneous adiabatic energy is constant. Our $F_z(t)$ dependence for each anticrossing has the form of a sine function. In the case of such a function, these two assumptions would approximately hold if the $F_z(t)$ oscillation amplitude was much greater than the F_z width of the anticrossing. However, in our case, these two are more or less comparable, and our use of the Runge-Kutta method to directly access the evolution of the wave function is justified.

VII. SUMMARY AND CONCLUSIONS

In the presented work, a system of double quantum dots, created in an InSb nanowire by application of an external

potential, was investigated. The energy spectrum of the system in a static electric field, applied in the direction of the wire, was obtained. The presence of non-axially-symmetric terms in the overall Hamiltonian leads to the formation of an avoided crossing in the spectrum, which involves two states of opposite spin states, in addition to the tunnel-coupling one. A scheme for reversing the spin state of a hole by manipulating the evolution with electric field was proposed, based on driving the hole state through two anticrossings. The results provided show that a perfect realization of the process, with exact control over the electric field, is possible, and the total process time is one order of magnitude smaller than the realization time of an alternative *classic* EDSR approach. The impact of imperfect control of the driving factor was studied with two simple models that correspond to two different kinds of errors, respectively.

ACKNOWLEDGMENTS

This work was supported by the São Paulo Research Foundation (FAPESP) postdoctoral grant; Process No. 2015/23786-5. Computations were performed at the LaS-CADo cluster (FT, Unicamp, Limeira SP).

APPENDIX A: THE TRANSFORMATION OF KOHN-LUTTINGER AND DRESSELHAUS HAMILTONIANS FROM $\langle 100 \rangle$ TO $\langle 111 \rangle$ DIRECTION

The four-band Kohn-Luttinger Hamiltonian for $\langle 100 \rangle$ crystal orientation is given by Eq. (3) and the Dresselhaus spin-orbit Hamiltonian in this orientation is given by Eq. (12). Please note that both are defined in the terms of \mathbf{k} and \mathbf{J} vectors. To transform the Hamiltonians to $\langle 111 \rangle$ crystal orientation, one needs to express the coordinates of these vectors for $\langle 100 \rangle$ in terms of their coordinates for $\langle 111 \rangle$ orientation. Within the scope of this Appendix, the $x, y, z, k_x, k_y, k_z, J_x, J_y, J_z$ symbols are used for the *old* crystal orientation and the $x', y', z', k'_x, k'_y, k'_z, J'_x, J'_y, J'_z$ symbols are used for the *new* one.

In x, y, z coordinates, the x' axis goes along the $[1, 1, -2]$ vector, the y' along the $[-1, 1, 0]$ vector, and z' along the $[1, 1, 1]$ vector. The related versors are

$$\begin{aligned}\hat{x}' &= \frac{\hat{x}}{\sqrt{6}} + \frac{\hat{y}}{\sqrt{6}} - \frac{2\hat{z}}{\sqrt{6}}, \\ \hat{y}' &= -\frac{\hat{x}}{\sqrt{2}} + \frac{\hat{y}}{\sqrt{2}}, \\ \hat{z}' &= \frac{\hat{x}}{\sqrt{3}} + \frac{\hat{y}}{\sqrt{3}} + \frac{\hat{z}}{\sqrt{3}},\end{aligned}\tag{A1}$$

and in consequence,

$$\begin{aligned}x &= \frac{x'}{\sqrt{6}} - \frac{y'}{\sqrt{2}} + \frac{z'}{\sqrt{3}}, \\ y &= \frac{x'}{\sqrt{6}} + \frac{y'}{\sqrt{2}} + \frac{z'}{\sqrt{3}}, \\ z &= -\sqrt{\frac{2}{3}}x' + \frac{z'}{\sqrt{3}}.\end{aligned}\tag{A2}$$

The u derivative in the $\{x', y', z'\}$ basis is equal to $\frac{\partial}{\partial u} = \frac{\partial x'}{\partial u} \frac{\partial}{\partial x'} + \frac{\partial y'}{\partial u} \frac{\partial}{\partial y'} + \frac{\partial z'}{\partial u} \frac{\partial}{\partial z'}$. After taking into account Eq. (A1),

the following relation for \vec{k} is obtained,

$$\begin{aligned} k_x &= \frac{1}{\sqrt{6}}k'_x - \frac{1}{\sqrt{2}}k'_y + \frac{1}{\sqrt{3}}k'_z, \\ k_y &= \frac{1}{\sqrt{6}}k'_x + \frac{1}{\sqrt{2}}k'_y + \frac{1}{\sqrt{3}}k'_z, \\ k_z &= -\sqrt{\frac{2}{3}}k'_x + \frac{1}{\sqrt{3}}k'_z. \end{aligned} \quad (\text{A3})$$

The spin vector in the old basis is equal to

$$\vec{J}_{\frac{3}{2}} = [J_x, J_y, J_z] = J_x \hat{x} + J_y \hat{y} + J_z \hat{z}, \quad (\text{A4})$$

and in the new basis the same vector is given by

$$\vec{J}_{\frac{3}{2}} = [J'_x, J'_y, J'_z] = J'_x \hat{x}' + J'_y \hat{y}' + J'_z \hat{z}'. \quad (\text{A5})$$

By comparing the right-hand sides of Eqs. (A4) and (A5) and taking into account Eq. (A1), the following expression for spin matrices can be obtained,

$$\begin{aligned} J_x &= \frac{1}{\sqrt{6}}J'_x - \frac{1}{\sqrt{2}}J'_y + \frac{1}{\sqrt{3}}J'_z, \\ J_y &= \frac{1}{\sqrt{6}}J'_x + \frac{1}{\sqrt{2}}J'_y + \frac{1}{\sqrt{3}}J'_z, \\ J_z &= -\sqrt{\frac{2}{3}}J'_x + \frac{1}{\sqrt{3}}J'_z. \end{aligned} \quad (\text{A6})$$

APPENDIX B: THE DRESSELHAUS HAMILTONIAN MATRICES FOR SPECIFIC J_z VALUES

The Dresselhaus Hamiltonian for the considered system [see Eqs. (13) and (14) and Table II] is defined in terms of \hat{k}_- , \hat{k}_+ , \hat{k}_\perp^2 , and \hat{k}_z operators that act on specific types of valence bands. Each single-band component of an \hat{H}_s eigenvector has an $e^{iJ_z^{\text{en}}\phi}$ type of angular dependency and thus a defined envelope angular momentum quantum number J_z^{en} [see Eqs. (6) and (9)]. In the case of matrix elements of the mentioned operators, for states with $(J_z^{\text{en}})_L$ and $(J_z^{\text{en}})_R$ quantum numbers, for $|L\rangle$ and $|R\rangle$ states, respectively, the result is nonzero only in the case of some relations of these numbers,

$$\begin{aligned} (J_z^{\text{en}})_R \neq (J_z^{\text{en}})_L + 1 &\Rightarrow \langle L|\hat{k}_-|R\rangle = 0, \\ (J_z^{\text{en}})_R \neq (J_z^{\text{en}})_L - 1 &\Rightarrow \langle L|\hat{k}_+|R\rangle = 0, \\ (J_z^{\text{en}})_R \neq (J_z^{\text{en}})_L &\Rightarrow \langle L|\hat{k}_\perp^2|R\rangle = 0, \\ (J_z^{\text{en}})_R \neq (J_z^{\text{en}})_L &\Rightarrow \langle L|\hat{k}_z|R\rangle = 0. \end{aligned} \quad (\text{B1})$$

The mentioned relations lead to a significant simplification of the Dresselhaus Hamiltonian for each specific pair of J_z numbers.

If we take into account only the states with a certain J_z , then the four envelope angular momentum quantum numbers J_z^{en} in $(\text{HH}\uparrow, \text{LH}\downarrow, \text{LH}\uparrow, \text{HH}\downarrow)$ basis are $(J_z - \frac{3}{2}, J_z + \frac{1}{2}, J_z - \frac{1}{2}, J_z + \frac{3}{2})$. For example, the $J_z = -\frac{3}{2}$ gives $(-3, -1, -2, 0)$ and for $J_z = +\frac{3}{2}$ the values $(0, 2, 1, 3)$ are obtained. The effective form of the Hamiltonian, for equal

J_z numbers of bra and ket states, becomes

$$\hat{H}'_D = \begin{pmatrix} 0 & \hat{O}_3 & \hat{O}_2 & \hat{O}_4 \\ \hat{O}_3^+ & 0 & \hat{O}_5 & \hat{O}_2 \\ \hat{O}_2^+ & \hat{O}_5^+ & 0 & -\hat{O}_3 \\ \hat{O}_4^+ & \hat{O}_2^+ & -\hat{O}_3^+ & 0 \end{pmatrix}, \quad (\text{B2})$$

with the operators defined as follows,

$$\begin{aligned} \hat{O}_2 &= -\frac{C_k}{\sqrt{3}}(i\hat{k}_-) + c_2\hat{k}_\perp^2(i\hat{k}_-) + c_4\hat{k}_z^2(i\hat{k}_-), \\ \hat{O}_3 &= -i\sqrt{3}c_6\hat{k}_z(i\hat{k}_-)^2, \quad \hat{O}_4 = c_6(i\hat{k}_-)^3, \\ \hat{O}_5 &= -C_k(i\hat{k}_+) - c_{10}\hat{k}_\perp^2(i\hat{k}_+) - c_{12}\hat{k}_z^2(i\hat{k}_+), \\ \hat{O}_2^+ &= \frac{C_k}{\sqrt{3}}(i\hat{k}_+) - c_2\hat{k}_\perp^2(i\hat{k}_+) - c_4\hat{k}_z^2(i\hat{k}_+), \\ \hat{O}_3^+ &= i\sqrt{3}c_6\hat{k}_z(i\hat{k}_+)^2, \quad \hat{O}_4^+ = -c_6(i\hat{k}_+)^3, \\ \hat{O}_5^+ &= C_k(i\hat{k}_-) + c_{10}\hat{k}_\perp^2(i\hat{k}_-) + c_{12}\hat{k}_z^2(i\hat{k}_-), \end{aligned} \quad (\text{B3})$$

and the constants c_2 - c_{12} as defined in Table II.

Analogously, the effective Hamiltonian for J_z and $J_z + 3$ (for bra and ket states, respectively) can be obtained. This corresponds, for example, to a pair of $J_z = -\frac{3}{2}$ and $J_z = +\frac{3}{2}$ states with the sets of envelope angular momentum quantum numbers J_z^{en} of $(-3, -1, -2, 0)$ and of $(0, 2, 1, 3)$, respectively. In this case, the effective Hamiltonian takes the form of

$$\hat{H}''_D = \begin{pmatrix} \hat{O}_1 & 0 & 0 & 0 \\ \hat{O}_3^+ & -a\hat{O}_1 & \hat{O}_5 & 0 \\ \hat{O}_2^+ & 0 & a\hat{O}_1 & 0 \\ \hat{O}_4^+ & \hat{O}_2^+ & -\hat{O}_3^+ & -\hat{O}_1 \end{pmatrix}, \quad (\text{B4})$$

with the operators defined as follows,

$$\begin{aligned} \hat{O}_1 &= -c_1(i\hat{k}_-)^3, \\ \hat{O}_5 &= ic_{11}\hat{k}_z(i\hat{k}_-)^2, \\ \hat{O}_2^+ &= ic_3\hat{k}_z\hat{K}_1^2, \\ \hat{O}_3^+ &= -\frac{C_k}{\sqrt{6}}\hat{K}_1 - c_5\hat{K}_3\hat{K}_1 - c_7\hat{K}_1\hat{k}_z^2, \\ \hat{O}_4^+ &= i\sqrt{2}C_k\hat{k}_z + ic_{13}\hat{k}_z\hat{K}_3 + ic_9\hat{k}_z^3, \end{aligned} \quad (\text{B5})$$

and the constants a and c_1 - c_{13} as defined in Table II.

Please note that in the cases of (i) J_z and $J'_z = J_z + 1$ (e.g., the $J_z = -\frac{5}{2}$, $J'_z = -\frac{3}{2}$ pair and the $J_z = \frac{1}{2}$, $J'_z = \frac{3}{2}$ pair), (ii) J_z and $J'_z = J_z + 2$ (e.g., the $J_z = -\frac{3}{2}$, $J'_z = \frac{1}{2}$ pair), and (iii) J_z and $J'_z = J_z + 4$ (e.g., the $J_z = -\frac{4}{2}$, $J'_z = \frac{3}{2}$ pair), the effective Dresselhaus Hamiltonian is zero and hence Dresselhaus-type spin orbit does not induce mixing of these states.

APPENDIX C: IMPLEMENTATION OF THE RUNGE-KUTTA METHOD

The Runge-Kutta method of the fourth order allows one to numerically solve the differential equation of the $\frac{dy}{dt} = f(t, y)$ kind with the starting condition $y_n = y(t_n)$. The value of the next step is calculated as follows,

$$y_{n+1} = y_n + \frac{k_1 + 2k_2 + 2k_3 + k_4}{6},$$

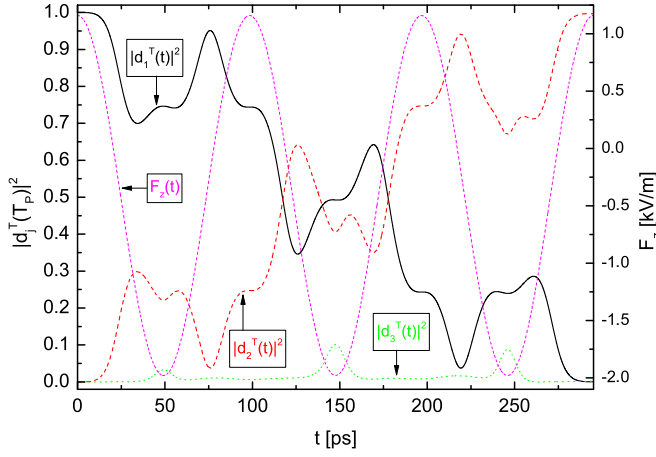


FIG. 9. Evolution for β transition; $p_s = 1.16$ kV/m, $p_b = -1.98$ kV/m, and $T_p = 295$ ps. Left axis: $|d_j(t)|^2$ projections for the time-dependent state $\Phi(\vec{r}, t)$ on the time-independent states $\Lambda_j(\vec{r})$. For $j = 4$ the projection is not shown as it is negligible for all $t \in (0, T_p)$. Right axis: $F_z(t)$ electric field drive.

$$\begin{aligned} k_1 &= \Delta_t f(t_n, y_n), \\ k_2 &= \Delta_t f\left(t_{n+\frac{1}{2}}, y_n + \frac{k_1}{2}\right), \\ k_3 &= \Delta_t f\left(t_{n+\frac{1}{2}}, y_n + \frac{k_2}{2}\right), \\ k_4 &= \Delta_t f(t_{n+1}, y_n + k_3). \end{aligned} \quad (\text{C1})$$

In the case of the Schrödinger equation

$$i\hbar \frac{\partial}{\partial t} |\Phi\rangle = \hat{H} |\Phi\rangle, \quad (\text{C2})$$

the $f(t, y)$ time derivative of Eq. (C1) is equal to

$$f(t, |\Phi\rangle) = \frac{\partial}{\partial t} |\Phi\rangle = -\frac{i}{\hbar} \hat{H} |\Phi\rangle, \quad (\text{C3})$$

and consequently

$$|\Phi\rangle_{n+1} = |\Phi\rangle_n + \frac{k_1 + 2k_2 + 2k_3 + k_4}{6}, \quad (\text{C4})$$

where

$$\begin{aligned} k_1 &= \Delta_t f(t_n, |\Phi\rangle_n) = -\frac{i\Delta_t}{\hbar} \hat{H}_n |\Phi\rangle_n, \\ k_2 &= \Delta_t f\left(t_{n+\frac{1}{2}}, |\Phi\rangle_n + \frac{k_1}{2}\right) = -\frac{i\Delta_t}{\hbar} \hat{H}_{n+\frac{1}{2}} \left(|\Phi\rangle_n + \frac{k_1}{2}\right), \\ k_3 &= \Delta_t f\left(t_{n+\frac{1}{2}}, |\Phi\rangle_n + \frac{k_2}{2}\right) = -\frac{i\Delta_t}{\hbar} \hat{H}_{n+\frac{1}{2}} \left(|\Phi\rangle_n + \frac{k_2}{2}\right), \\ k_4 &= \Delta_t f(t_{n+1}, |\Phi\rangle_n + k_3) = -\frac{i\Delta_t}{\hbar} \hat{H}_{n+1} (|\Phi\rangle_n + k_3). \end{aligned} \quad (\text{C5})$$

Due to code implementation purposes, it is convenient to redefine the algorithm in the terms of

$$\begin{aligned} |x_1\rangle &= |\Phi\rangle_n + \frac{k_1}{2} = |\Phi\rangle_n - \frac{i\Delta_t}{2\hbar} \hat{H}_n |\Phi\rangle_n, \\ |x_2\rangle &= |\Phi\rangle_n + \frac{k_2}{2} = |\Phi\rangle_n - \frac{i\Delta_t}{2\hbar} \hat{H}_{n+\frac{1}{2}} |x_1\rangle, \end{aligned}$$

$$\begin{aligned} |x_3\rangle &= |\Phi\rangle_n + k_3 = |\Phi\rangle_n - \frac{i\Delta_t}{\hbar} \hat{H}_{n+\frac{1}{2}} |x_2\rangle, \\ |x_4\rangle &= \frac{k_4}{2} = -\frac{i\Delta_t}{2\hbar} \hat{H}_{n+1} |x_3\rangle, \end{aligned} \quad (\text{C6})$$

and that leads to

$$|\Phi\rangle_{n+1} = \frac{|x_1\rangle + 2|x_2\rangle + |x_3\rangle + |x_4\rangle - |\Phi\rangle_n}{3}. \quad (\text{C7})$$

As the evolving wave function $|\Phi\rangle$ is defined as the superposition of basis states [see Eq. (18)], the way to obtain the evolution algorithm for a given projection d_j is to multiply Eq. (C7) by the ket j th basis state $\langle \Lambda_j(F_z = 0) |$ from the left-hand side. This leads to the following formula, in atomic units,

$$\begin{aligned} d_j(t_{n+1}) &= \frac{[x_1]_j + 2[x_2]_j + [x_3]_j + [x_4]_j - d_j(t_n)}{3}, \\ [x_1]_j &= d_j(t_n) - \frac{i\Delta_t}{2} \langle \Lambda_j(F_z = 0) | \hat{H}_n | \Phi\rangle_n, \\ [x_2]_j &= d_j(t_n) - \frac{i\Delta_t}{2} \langle \Lambda_j(F_z = 0) | \hat{H}_{n+\frac{1}{2}} | x_1\rangle, \\ [x_3]_j &= d_j(t_n) - i\Delta_t \langle \Lambda_j(F_z = 0) | \hat{H}_{n+\frac{1}{2}} | x_2\rangle, \\ [x_4]_j &= -\frac{i\Delta_t}{2} \langle \Lambda_j(F_z = 0) | \hat{H}_{n+1} | x_3\rangle, \end{aligned} \quad (\text{C8})$$

where $[x_i]_j = \langle \Lambda_j(F_z = 0) | x_i\rangle$ and $j \in \Phi_{\text{basis}}$.

APPENDIX D: DETAILED OPTIMIZATION OF THE DRIVING SIGNAL

1. Transfer using the larger avoided crossing

For this part of the transfer, an initial state identical to the ground state $d_1(0) = 1$ is assumed and our goal is to maximize the first excited state projection after the evolution $|d_2(T_p)|^2$ [see Eq. (18)]. The following function was accepted as the

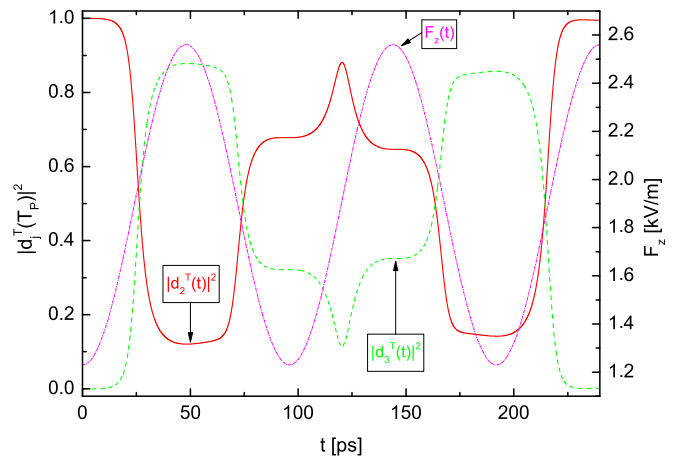


FIG. 10. Evolution for δ transition; $p_s = 1.23$ kV/m, $p_f = 2.56$ kV/m, and $T_p = 240$ ps. Left axis: $|d_j(t)|^2$ projections for the time-dependent state $\Phi(\vec{r}, t)$ on the time-independent states $\Lambda_j(\vec{r})$. For $j \in \{1, 4\}$ the projections are not shown as they are negligible for all $t \in (0, T_p)$. Right axis: $F_z(t)$ electric field drive.

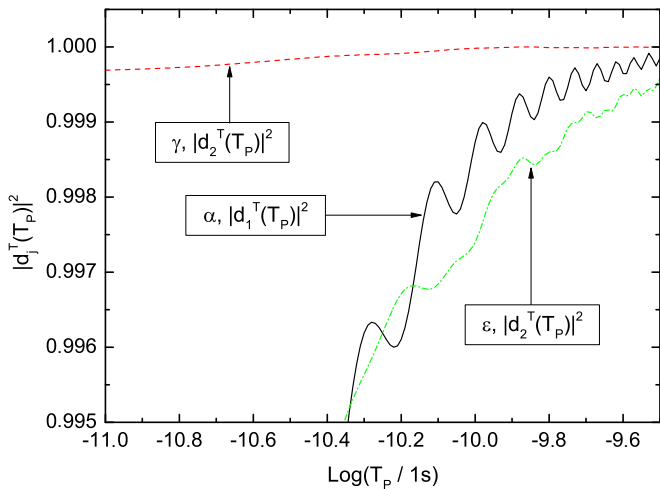


FIG. 11. Optimization of the T_p parameter for α , γ , and ϵ transitions. The $|d_j(T_p)|^2$ projection for the time-dependent state $\Phi(\vec{r}, t)$ on the j th time-independent state $\Lambda_j(\vec{r})$ as a function of evolution time T_p , where $j = 1$ for α and $j = 2$ for γ and ϵ .

driving element for the β transition [see Fig. 3(b)],

$$F_z(t) = \frac{p_s + p_b}{2} + \frac{p_s - p_b}{2} \cos\left(\frac{6\pi t}{T_p}\right), \quad (\text{D1})$$

where p_s is the initial and final value of the F_z pulse, p_b is the bouncing point on the $F_z < 0$ side of the avoided crossing, and T_p is the evolution time. The function (D1) has three parameters, p_s , p_b , and T_p . A three-dimensional optimization of these parameters has been done in order to maximize the efficiency of the transfer. The method used was a grid search with a mesh spacing of $\Delta p_s = \Delta p_b = 0.01$ kV/m and with $\Delta \log_{10}\left(\frac{T_p}{1\text{s}}\right) = 0.01$. The ranges for the search were chosen so that the values of p_s and p_b ensure the correct overlap of the $F_z(t)$ pulse range and the range of the A anticrossing. The evolution time T_p corresponds to the time scale of the process. The points on the search grid were chosen to lie in equal distances of $\log_{10}\left(\frac{T_p}{1\text{s}}\right)$ due to the need to search among more than one order of magnitude. The obtained values of the parameters are $p_s = 1.16$ kV/m, $p_b = -1.98$ kV/m, and $T_p = 295$ ps. The optimal value $|d_2(T_p)|^2 > 0.996$ was

obtained. This value is very close to unity and it is sufficient for the realization of the intended goal. The range of the pulse is marked in Fig. 3(b) as F_A .

The evolution for the set of parameters obtained in the optimization is presented in Fig. 9. The evolving state starts in the ground state, $d_1(0) = 1$. As the impulse $F_z(t)$ starts to diverge from the initial value p_s , the $|d_1|^2$ drops and $|d_2|^2$ grows by an equal amount. In the regions where F_z is close to p_b , the second excited state is active in the process with $|d_3(0)|^2 > 0$ storing a bit of the evolving wave function for a small moment. This is due to the fact that p_b lies relatively close to the C anticrossing that involves the first and the second excited levels [see F_A in Fig. 3(b)]. As the impulse begins to go back from p_b to p_s , the transfer continues. The process repeats three times until the evolving state is transferred almost completely to the first excited time-independent level, $|d_2(T_p)|^2 \approx 1$. The first movement through the avoided crossing from p_s to p_b and back results in transferring 0.25 of the initial $|d_1|^2$ projection to the $|d_2|^2$ one. The second go increases $|d_2|^2$ by an additional 0.5 and the last one results in transferring the remaining 0.25 from $|d_1|^2$.

2. Transfer using the smaller avoided crossing

At this stage the initial state of the system is equal to the first excited time-independent state, $d_2(0) = 1$. We seek to maximize $|d_2(T_p)|^2$, that is, the projection of the same kind after the evolution [see Eq. (18)]. The time-dependent electric field for the δ transition [see Fig. 3(b)] is given by

$$F_z(t) = \frac{p_s + p_f}{2} + \frac{p_s - p_f}{2} \cos\left(\frac{5\pi t}{T_p}\right), \quad (\text{D2})$$

where p_s is the initial value of the F_z pulse, p_f is the final value, and T_p is the evolution time. The function (D2) has three parameters, p_s , p_f , and T_p . A three-dimensional optimization of these parameters has been done in order to maximize the efficiency of the transfer, with the grid search method similar to the one described above, for the case of the larger anticrossing. We have accepted (1.57, 2.3) kV/m as a rough estimate for the F_z range of the considered anticrossing. The three-dimensional optimization yielded the following values for the parameters,

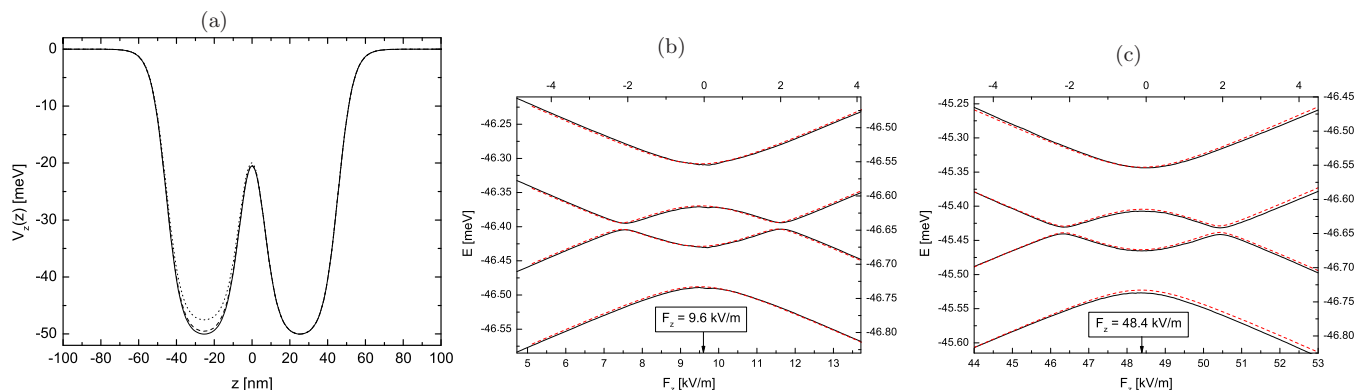


FIG. 12. (a) The confinement potential along the z axis with no asymmetry (solid line), 1% asymmetry (dashed line), and 5% asymmetry (dotted line). (b), (c) (Bottom F_z scale, left energy scale, solid line) Hole energy spectrum of the system with non-axially-symmetric terms included with (b) 1% asymmetry, (c) 5% asymmetry; (top F_z scale, right energy scale, dotted line) hole energy spectrum of the system with non-axially-symmetric terms included without the z -axis asymmetry, for comparison.

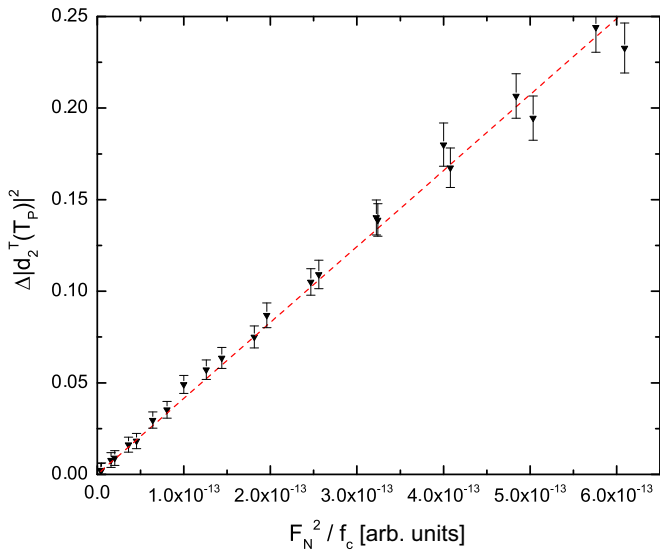


FIG. 13. The loss in final $|d_2|^2$ projection for the RTN noise simulation as a function of the $\frac{F_N^2}{f_c}$ argument. The line is a linear fit to the data.

$p_s = 1.23$ kV/m, $p_f = 2.56$ kV/m, and $T_P = 240$ ps. An optimal value $|d_2(T_P)|^2 > 0.995$ was obtained. This value is very close to unity and it is sufficient for the realization of the intended goal. The range of the pulse is shown in Fig. 3(b) as the δ stage.

The evolution for the set of parameters obtained from the optimization is presented in Fig. 10. The evolving state starts in the first excited state $d_2(0) = 1$. The driving field $F_z(t)$ has a minimal value $p_s = 1.23$ kV/m for $t \in \{0, 96 \text{ ps}, 192 \text{ ps}\}$, which corresponds to the hole being driven to the *left*-hand side of the avoided crossing D in Fig. 3(b). For this sequence of time values a characteristic behavior can be observed: The corresponding values of $|d_2|^2$ are systematically decreasing and the corresponding values of $|d_3|^2$ are systematically increasing. On the other hand, when the driving field $F_z(t)$ has a maximal value $p_f = 2.56$ kV/m for $t \in \{48 \text{ ps}, 144 \text{ ps}, T_P\}$, the hole system is on the *right*-hand side of the mentioned avoided crossing. For this sequence of time values the corresponding values of $|d_2|^2$ are systematically increasing and the corresponding values of $|d_3|^2$ are systematically decreasing. This marks the transition from the system in which the hole occupies the first excited state $\Psi_2(\vec{r})$ on the *left*-hand side and it occupies the second excited state $\Psi_3(\vec{r})$ on the *right*-hand side, to the system with reversed occupation characteristics.

3. α , γ , and ϵ transfers

The optimization of the transfers through both avoided crossings yields the border F_z values for other stages of the process [see Fig. 3(b)]. Explicitly, the α transfer should drive the system from $F_z = 4$ kV/m to $F_z = 1.16$ kV/m, the γ transfer needs to initiate at $F_z = 1.16$ kV/m and end at $F_z = 1.23$ kV/m, and the ϵ transfer is to be done between electric field values of $F_z = 2.56$ kV/m and $F_z = 4$ kV/m. For each of these stages, the hole state occupation should remain the same. The only limitation of the process is that it should be done slowly enough to enable the wave function

to accommodate for the change in F_z . In other words, these transfers should be made quasiadiabatically.

The following $F_z(t)$ function driving the system from p_s to p_f has been adopted,

$$F_z(t) = p_s + (p_f - p_s) \frac{t}{T_P}, \quad (\text{D3})$$

which (if the p_s and p_f values are already set) has only one free parameter T_P , i.e., the evolution time. The results of optimization of this parameter for α , γ , and ϵ transfers are presented in Fig. 11. T_P should be as small as possible to make the process fast, while it also should guarantee a very good transfer effectiveness. The evolution time adopted for the α step is $T_P = 10^{-9.9} \text{ s} = 125$ ps, for the γ step it is $T_P = 10^{-10.3} \text{ s} = 50$ ps, and for the ϵ step it is $T_P = 10^{-9.825} \text{ s} = 150$ ps. In each case the chosen time allows for a transition effectiveness > 0.995 .

APPENDIX E: THE ASYMMETRIC SYSTEM

The quantum dot confinement that was considered in the main part of the work is symmetric with respect to reversing the z axis. In reality, it is probable that the perfect symmetry in this regard cannot be maintained, due to technological limitations. In this Appendix, we present the study of an impact of a small asymmetry in the confinement potential on the behavior of the system. Two cases have been considered: (i) The $z < 0$ dot is 1% shallower than the $z > 0$ dot, and (ii) the $z < 0$ dot is 5% shallower than the $z > 0$ dot. The z -axis confining potential has the form of

$$V_z(z) = V_0 [x_{as} V_z^d(z_l) + V_z^d(z_r)], \quad (\text{E1})$$

where $x_{as} \in \{0.95, 0.99\}$ and the other symbols are as defined in Eq. (2).

The shapes of the z -axis confinement potentials are presented in Fig. 12(a) and the energy spectra of the system, with the nonaxial part taken into consideration, are presented in Figs. 12(b) and 12(c). The potential with the smaller asymmetry is almost identical to the symmetric one and the potential with the bigger asymmetry is easily discernible from the symmetric one [see Fig. 12(a)]. However, the spectra in both cases have nearly the same character as the one for the symmetric system [compare solid and dashed lines in Figs. 12(b) and 12(c)]. The only difference is the shift of the whole spectrum in terms of the electric field and energy, but the shape and the size remain the same. The position of the middle of the tunneling anticrossing is at about $F_z = 0$ for the system considered in the main part of this work, but it is shifted to about $F_z = 9.6$ kV/m in the case of 1% asymmetry [see Fig. 12(b)] and to $F_z = 48.4$ kV/m in the case of 5% asymmetry [see Fig. 12(c)]. The results for the case when the $z > 0$ dot is shallower than the $z < 0$ one (not shown) are nearly the same, with the exception that the electric field shift is negative. In conclusion, the impact of a small asymmetry on the behavior of the system is minimal and the evolution research can be done for the symmetric system.

APPENDIX F: THE ANALOGY BETWEEN THE HIGH-FREQUENCY RTN REGIME AND THE MOTIONAL NARROWING

The motional narrowing is a decrease in the linewidth of a resonant frequency, that is, an effect of the motion in an inhomogeneous system. For a description of the phenomenon in the case of magnetic resonance, see, e.g., Ref. [30]. In a very simple model it can be described by the following formula (see Ref. [30], p. 213),

$$\frac{1}{T_2} = \gamma_n^2 H_z^2 \tau, \quad (\text{F1})$$

where H_z is the magnetic field amplitude, τ is the lifetime of an \vec{H} orientation, T_2 is the relaxation time, and γ_n^2 is a constant. In our system, the analog of H_z is the RTN amplitude of the

electric field F_N . The equivalent of the reverse of τ is the noise frequency f_c . As a first approximation, we assume that the left-hand side $\frac{1}{T_2}$ corresponds to the final efficiency loss of the transfer $\Delta|d_2(T_P)|^2$. This leads to the following equation,

$$\Delta|d_2(T_P)|^2 = C \frac{F_N^2}{f_c}. \quad (\text{F2})$$

The results of the RTN simulation for the highest frequency and small amplitude regime, presented as a function of the $\frac{F_N^2}{f_c}$ argument, are given in Fig. 13. The corresponding area is marked in Fig. 7 with a square. The linear function fits the data quite well for the considered range of parameters.

-
- [1] V. N. Golovach, M. Borhani, and D. Loss, *Phys. Rev. B* **74**, 165319 (2006).
- [2] Y. Tokura, W. G. van der Wiel, T. Obata, and S. Tarucha, *Phys. Rev. Lett.* **96**, 047202 (2006).
- [3] K. C. Nowack, F. H. L. Koppens, Y. V. Nazarov, and L. M. K. Vandersypen, *Science* **318**, 1430 (2007).
- [4] E. A. Laird, C. Barthel, E. I. Rashba, C. M. Marcus, M. P. Hanson, and A. C. Gossard, *Phys. Rev. Lett.* **99**, 246601 (2007).
- [5] M. Pioro-Ladriere, T. Obata, Y. Tokura, Y. S. Shin, T. Kubo, K. Yoshida, T. Taniyama, and S. Tarucha, *Nat. Phys.* **4**, 776 (2008).
- [6] S. Nadj-Perge, S. M. Frolov, E. P. A. M. Bakkers, and L. P. Kouwenhoven, *Nature (London)* **468**, 1084 (2010).
- [7] M. D. Schroer, K. D. Petersson, M. Jung, and J. R. Petta, *Phys. Rev. Lett.* **107**, 176811 (2011).
- [8] S. Nadj-Perge, V. S. Pribiag, J. W. G. van den Berg, K. Zuo, S. R. Plissard, E. P. A. M. Bakkers, S. M. Frolov, and L. P. Kouwenhoven, *Phys. Rev. Lett.* **108**, 166801 (2012).
- [9] S. M. Frolov, J. Danon, S. Nadj-Perge, K. Zuo, J. W. W. van Tilburg, V. S. Pribiag, J. W. G. van den Berg, E. P. A. M. Bakkers, and L. P. Kouwenhoven, *Phys. Rev. Lett.* **109**, 236805 (2012).
- [10] K. D. Petersson, L. W. McFaul, M. D. Schroer, M. Jung, J. M. Taylor, A. A. Houck, and J. R. Petta, *Nature (London)* **490**, 380 (2012).
- [11] V. S. Pribiag, S. Nadj-Perge, S. M. Frolov, J. W. G. van den Berg, I. van Weperen, S. R. Plissard, E. P. A. M. Bakkers, and L. P. Kouwenhoven, *Nat. Nanotechnol.* **8**, 170 (2013).
- [12] S. N. Shevchenko, S. Ashhab, and F. Nori, *Phys. Rep.* **492**, 1 (2010).
- [13] J. Stehlik, M. D. Schroer, M. Z. Maialle, M. H. Degani, and J. R. Petta, *Phys. Rev. Lett.* **112**, 227601 (2014).
- [14] J. Stehlik, M. Z. Maialle, M. H. Degani, and J. R. Petta, *Phys. Rev. B* **94**, 075307 (2016).
- [15] J. Danon and M. S. Rudner, *Phys. Rev. Lett.* **113**, 247002 (2014).
- [16] H. Ribeiro, J. R. Petta, and G. Burkard, *Phys. Rev. B* **82**, 115445 (2010).
- [17] H. Ribeiro, J. R. Petta, and G. Burkard, *Phys. Rev. B* **87**, 235318 (2013).
- [18] J. R. Petta, H. Lu, and A. C. Gossard, *Science* **327**, 669 (2010).
- [19] K. Ono, G. Giavaras, T. Tanamoto, T. Ohguro, X. Hu, and F. Nori, *Phys. Rev. Lett.* **119**, 156802 (2017).
- [20] S. L. Chuang, *Physics of Photonic Devices*, 2nd ed. (Wiley, New York, 2009).
- [21] Z. Ikonić, V. Milanović, and D. Tjapkin, *Phys. Rev. B* **46**, 4285 (1992).
- [22] R. H. Henderson and E. Towe, *J. Appl. Phys.* **78**, 2447 (1995).
- [23] The explicit formula for this function is $s_p(z) = -\frac{818}{z} + 57.6 - 1.60z + 2.34 \times 10^{-2}z^2 - 1.87 \times 10^{-4}z^3 + 7.72 \times 10^{-7}z^4 - 1.29 \times 10^{-9}z^5$.
- [24] J. Planelles and J. I. Climente, *J. Phys.: Condens. Matter* **25**, 485801 (2013).
- [25] The maximal value of B_z considered is 200 mT, for which the additional confinement potential would be equal to 0.11 meV for heavy holes and 0.04 meV in the case of light holes. These values can be omitted when compared with the lateral confinement resulting from the wire-vacuum boundary.
- [26] C. Segarra, J. I. Climente, F. Rajadell, and J. Planelles, *J. Phys.: Condens. Matter* **27**, 415301 (2015).
- [27] R. Winkler, *Spin-Orbit Coupling Effects in Two Dimensional Electron and Hole Systems* (Springer, Berlin, 2003).
- [28] I. Vurgaftman, J. R. Meyer, and L. R. Ram-Mohan, *J. Appl. Phys.* **89**, 5815 (2001).
- [29] L. K. Castelano, F. F. Fanchini, and K. Berrada, *Phys. Rev. B* **94**, 235433 (2016).
- [30] C. P. Slichter, *Principles of Magnetic Resonance*, 3rd ed. (Springer, New York, 1990).